

University of Groningen

Toward observable UHVCVD

Dresscher, Martijn; Jayawardhana, Bayu; Kooi, Bart; Scherpen, Jacquélien M.A.

Published in:
 Mechatronics

DOI:
[10.1016/j.mechatronics.2020.102427](https://doi.org/10.1016/j.mechatronics.2020.102427)

IMPORTANT NOTE: You are advised to consult the publisher's version (publisher's PDF) if you wish to cite from it. Please check the document version below.

Document Version
 Publisher's PDF, also known as Version of record

Publication date:
 2020

[Link to publication in University of Groningen/UMCG research database](#)

Citation for published version (APA):

Dresscher, M., Jayawardhana, B., Kooi, B., & Scherpen, J. M. A. (2020). Toward observable UHVCVD: Modeling of flow dynamics and AAS partial pressure measurement implementation. *Mechatronics*, 71, Article 102427. <https://doi.org/10.1016/j.mechatronics.2020.102427>

Copyright

Other than for strictly personal use, it is not permitted to download or to forward/distribute the text or part of it without the consent of the author(s) and/or copyright holder(s), unless the work is under an open content license (like Creative Commons).

The publication may also be distributed here under the terms of Article 25fa of the Dutch Copyright Act, indicated by the "Taverne" license. More information can be found on the University of Groningen website: <https://www.rug.nl/library/open-access/self-archiving-pure/taverne-amendment>.

Take-down policy

If you believe that this document breaches copyright please contact us providing details, and we will remove access to the work immediately and investigate your claim.

Downloaded from the University of Groningen/UMCG research database (Pure): <http://www.rug.nl/research/portal>. For technical reasons the number of authors shown on this cover page is limited to 10 maximum.



Toward observable UHVCVD: Modeling of flow dynamics and AAS partial pressure measurement implementation[☆]

M. Dresscher^{*,1}, B. Jayawardhana, B.J. Kooi, J.M.A. Scherpen

Faculty of Science and Engineering, University of Groningen, Nijenborgh 4, 9747AG Groningen, The Netherlands

ARTICLE INFO

Keywords:

Ultra-high vacuum
Chemical vapor deposition
Atomic absorption spectroscopy
Process control
Modeling for control
Nonlinear systems
Free molecular flow
Vapor pressure

ABSTRACT

Ultra-high vacuum chemical vapor deposition is a thin film deposition process that features excellent film purity, but is sensitive to the processing variations (such as, the precursors and their dispensers, the reactor's initial condition, etc.). In this paper, we present the design of a ultra-high vacuum chemical vapor deposition reactor with *in situ* partial pressure atomic absorption spectroscopy measurement that improves reproducibility and observability of such a process. Our main contributions are: (i) a conceptual control systems design of ultra-high vacuum chemical vapor deposition; (ii) atomic absorption spectroscopy based sensor design for the real-time *in situ* partial pressure measurements; (iii) a flux dynamical model; (iv) experimental reactor design; and (v) experimental validation of model components and the atomic absorption spectroscopy measurement technique. Our results show that the proposed sensor systems are able to provide real-time measurements of the partial pressure inside the reactor and our proposed flux dynamical model agrees with the measured partial pressure. The latter allows us to use it in the design of model-based output feedback control of the partial pressure.

1. Introduction

Chemical vapor deposition (CVD) is a highly versatile and widely used thin-film growth technique, with applications in semiconductor processing [1]. CVD processes typically feature excellent film uniformity, conformality, compatibility with large area processing and relatively low apparatus costs compared with physical vapor deposition techniques. Differences between CVD processes are characterized by processing conditions, chemical activation methods or precursor material characteristics. For example, we distinguish between atmospheric pressures CVD (APCVD) [2] and low pressure CVD (LPCVD) [3]; hot wall [4] and cold wall [5] CVD; plasma enhanced CVD (PECVD) [6]; metal–organic CVD (MOCVD) [7] and many others. Each type of CVD process has distinct advantages and drawbacks and the selection of process type is completely application dependent. The specific type of CVD process that is of interest to us is ultra-high vacuum CVD (UHVCVD). This process has been introduced in the literature by [8] and a well-known application is the deposition of SiGe for microelectronics manufacturing [9–11]. UHVCVD is a candidate process type for precursors that have a tendency to bind with residual gases or for applications with extraordinary high purity demands. It is furthermore reported that UHVCVD has a potential for depositing with reduced temperature in comparison with higher pressures, which in

turn can lead to reduced auto-doping for specific applications [10]. We allow for precursor transport both as a molecular beam and through a background pressure in UHVCVD. Binding of the precursors to the substrate through chemical reactions formally qualifies the process as a CVD process, while the binding to the substrate is physical in physical vapor deposition (PVD) processes. In the latter case, there will not be a significant pressure buildup and evaporation needs to be performed in line-of-sight, e.g. through a molecular beam. When all precursors are transported as a molecular beam, the process will become similar to a thermal evaporation process such as molecular beam epitaxy (MBE) [12,13]. Allowing for transport through a background pressure has two potential benefits, namely: (i) the free molecular flow transport regime that is present in UHVCVD processes allows for highly uniform depositions over large surfaces, due to the undirected nature of the fluxes, and (ii) the indirect transportation from the reactant sources allows for the removal of undesired atoms or molecules that become released with the precursors before they reach the substrate, and thus allowing for a further reduction of deposition impurities. Prior contributions to the mechatronic system design and control for UHVCVD are not directly visible in the literature. The most relevant publications consider such principles for MBE processes, which in turn do not consider the build-up of precursor background pressures for

[☆] This paper was recommended for publication by Associate Editor Kam K. Leang.

* Corresponding author.

E-mail address: martjndresscher@posteo.net (M. Dresscher).

¹ Current affiliation: TNO Optomechatronics, Stieltjesweg 1, 2628CK Delft, The Netherlands.

depositions. Our contribution to the state-of-the-art accordingly focuses on applying control design principles for such background pressures.

Let us shortly discuss some of the challenges associated with UHVCVD. Desirably, the process allows for the deposition of thin films with arbitrary material properties like composition and crystal structure. The occurring reactions are principally a result of reactant availability and temperature, in accordance with the law of mass action and as studied in [9] for the example of *SiGe*. Accordingly, for any specific reaction to occur, desired amounts of reactants and reaction temperatures can be attained so that (epitaxial) growth of the desired compound is maximized. However, desired amounts of reactants and reaction temperatures are often unknown because the vacuum conditions and high operating temperatures restrict placement of *in situ* sensors. *Furthermore, knowledge on the fundamental processing dynamics is often lacking, causing operating recipes to be determined empirically with the limited data available.* This is further complicated by run-to-run variations of the substrate surface geometry, precursor evaporation sources and reactor conditions, in turn causing major variations in the chemistry occurring at nanoscale. These effects result in fluctuations in end-product quality between runs while applying the same operating recipe. Reproducibility and process optimization are therefore difficult. Such observations are in line with a more general evaluation of semiconductor and thin film processes by [14]. As emphasized by [14], a way to deal with these challenges is by implementing both real-time and run-to-run control. To develop these controllers, a starting point has to be made with enabling real-time measurements of relevant reactor states. The relevant reactor states for a UHVCVD process are accordingly the background pressures (or magnitude of the fluxes directed at the substrate), the substrate temperature and the layer characteristics. These measurements subsequently need to be connected to the reactor inputs or actuators through models suitable for controller design.

The following contributions are presented in this paper: (i) a conceptual mechatronic control systems design of UHVCVD; (ii) sensor design for the real-time *in situ* partial pressure measurements; (iii) a flux dynamical model that describes the relationship between reactor's inputs, the partial pressure measurement and the chemical reaction kinetics; (iv) experimental setup design for the validation of sensor design and model; and (v) experimental results assessing the quality of the measurement, the fluxes model and a benchmark moles model. Our experimental validation is performed in the vapor pressure regime. Obtaining insights in two important modeling components, namely the chemical reactions and the precursor evaporation process, falls outside the scope of the experimental part of this paper. The obtained results highlight the efficacy of the mechatronics design approach through an improvement of reproducibility and observability for UHVCVD processes.

The remainder of the paper is structured as follows. In Section 2 we present our conceptual mechatronic control system design for UHVCVD and our motivation for the design of AAS-based partial pressure sensor systems. Section 3 is subsequently used to present the flux dynamical model that describes the dynamics of partial pressure in the reactor. In this section we furthermore introduce the relevant mathematical notation used in this model. Section 4 is used to present experimental reactor design, AAS-based partial pressure sensor system design, fluxes model and a benchmark moles model. The experiment specific mathematical notation is furthermore introduced here. We then use Section 5 to present and discuss the experimental results. Lastly, Section 6 rounds up with the conclusions. An overview of the mathematical notation used in this paper is shown in Table 1, where the measured variables are also highlighted.

2. Toward an observable UHVCVD

We will use this section to discuss real-time control problems in UHVCVD process and to present our conceptual control systems design.

Table 1

List of symbols. The bold descriptions are the directly measured variables in the experiment presented in this paper.

P	Pressure in Pa
V	Volume in m^3
N	Number of moles
R	Ideal gas constant in $\frac{\text{J}}{\text{mol K}}$
T_a	Temperature of the atom cloud in K
\dot{N}_{in}	Number of moles per second entering the volume
$\dot{N}_s(\cdot)$	Sorption function for moles model
\dot{N}_{out}	Number of moles per second leaving the volume
\mathbb{M}	Deposition chamber inner surface
x	Flux in moles per second, arriving at a surface ω
ω_1, ω_2	Discrete surfaces, are in \mathbb{M}
p^A	Knudsen cosine law transfer matrix
s	Moles to a surface ω
$G(\cdot), g(\cdot)$	Input functions
u	Evaporation source input
A	Time corrected transfer matrix, δp^A
δ	Time scale constant
L	Leakage matrix
$f(\cdot)$	Sorption function for fluxes model
z	Time derivative of s
y	Fluxes model partial pressure output in Pa
$h(\cdot)$	Output function
M	Molar mass in $\frac{\text{kg}}{\text{mol}}$
\mathbb{I}	n -length column vector of ones
ℓ	Symmetric path length matrix
v	Average speed of atoms in the atom cloud
$p_{d\omega_1}(d\omega_2)$	Fraction of particles leaving $d\omega_1$ in direction $d\omega_2$
$d\omega_1, d\omega_2$	Infinitesimal surfaces associated to ω_1 and ω_2
$\theta_{d\omega_1}, \Phi_{d\omega_1}$	Angles associated with orientation of $d\omega_1$
$\text{dist}(\cdot, \cdot)$	Euclidean distance between two points
q	Directed flux matrix between surfaces
λ	AAS absorbance, based on Q signals, see (15)
Q_{in}	Derived light intensity entering the atom cloud
Q_{out}	Derived light intensity exiting the atom cloud
Q_s	Measured light intensity with shutter open
Q_b	Measured light intensity with shutter closed
Q_{ref}	Measured baseline light intensity
L	Light path length through atom cloud
k	Absorbing coefficient
Λ	AAS determined pressure in Pa, based on λ
$\Psi(\cdot)$	Function mapping λ to Λ
P_{Na}	Sodium vapor pressure in Pa, based on T_c
T_c	Measured cold spot temperature in K
$\xi(\cdot)$	Semi-empirical mapping of T_c to P_{Na}
T_r	Reference cold spot temperature input signal
\hat{u}	Model cold spot temperature input, $\hat{T}_r = \hat{u}$
b_1, b_2, b_3	Scalars in $f(\cdot)$ for simulation
α, β	Scalars in $\dot{N}_s(\cdot)$ for simulation
\bar{y}	Moles model partial pressure output in Pa
e_A	Normalized absolute error of Λ w.r.t. P_{Na}
$e_{\bar{y}}$	Normalized absolute error of \bar{y} w.r.t. P_{Na}
e_y	Normalized absolute error of y w.r.t. P_{Na}

Such a conceptual control system motivates the aim of this paper to contribute to an observable UHVCVD system, the observed states can the subsequently be used for controller design. We will furthermore motivate our choice of the AAS measurement for the real-time *in situ* partial pressure sensor system.

2.1. Control for UHVCVD

Let us consider the conceptual control system as shown in Fig. 1. This scheme utilizes both run-to-run and real-time controllers, in accordance with [14]. For background reading on run-to-run control we refer the interested reader to [15]. The real-time controllers generate control signals for the precursor evaporation sources, the substrate temperature and the reactor temperature.

A candidate control type for this process is model-predictive control, as is demonstrated for an atmospheric pressure CVD process by [16]. Such controllers require dynamical models that can predict future states of the system. The predictive models are continuously updated with

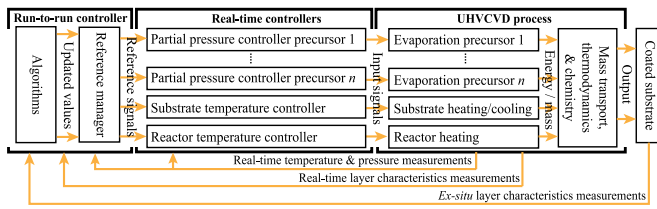


Fig. 1. Our conceptual mechatronic control system of a fully automated UHVCVD process is shown. The run-to-run controller consists of a learning algorithm and a reference manager. The reference manager generates reference signals for the real-time controllers, which can be event based and thus dependent on real-time measurements. This is updated between runs by a learning algorithm, based on *ex situ* measurements. The real time controllers provide control input signals for various actuators of the UHVCVD system, based on the reference signal. Lastly, the UHVCVD system produces a coated substrate which can be analyzed *ex situ*.

new measurement data for the recalculation of optimal control inputs that minimize a given cost function in a receding horizon manner. In this regards, designing a controlled UHVCVD processes is an integrated design problem of the reactor, sensors, actuators, a model and the controllers. The reactor, sensor and actuator design should be integrated in such a way, that a fairly low complexity model can relate (past) input variables, such as currents and voltages, to the present and future values of temperatures and precursor fluxes (in particular to the substrate). Such a model should moreover be designed so that it subsequently allows for (low complexity) control design.

In this work the integrated design of both reactor (hardware) and model for UHVCVD is given special attention because existing solutions for different types of CVD processes are not directly applicable to the UHVCVD process. For example, in [17] temperature measurement and control techniques are reviewed for rapid thermal CVD. However, since no convection occurs in vacuum, the dynamics of the aforementioned case will be different to that of UHVCVD. In [18–20], modeling and optimization of atomic layer deposition (ALD) processes are presented. In this case, the gas flow dynamics in trenches of ALD processes match the gas flow dynamics of UHVCVD processes. However, these studies are focused on knowing when step coverage² is achieved and not on facilitating controller design.

2.2. Real-time partial pressure sensor systems

The measurable state variables that are relevant for realizing an observable³ UHVCVD process are: (i) temperatures; (ii) film characteristics (such as, thickness, layer composition, etc.); and (iii) precursor partial pressures (or fluxes) at the substrate. The first and third variables together affect the chemical reactions that are the depositions, which in turn affects the second one. This is in accordance with the modeling for UHVCVD as in [9]. Measuring temperatures can be done through contact (thermocouple) and optically (pyrometer). Both of these methods are well established and compatible with UHV. Temperature control is typically performed by placing PID-controlled heating or cooling elements at locations of interest, such as the substrate. Such a form of control is rudimentary but works well, in particular in combination with a reference manager. Measuring layer characteristics (the second measured state variable) can be done optically through the use of ellipsometry, reflection or transmission measurements (as for example implemented in [16]). The techniques are well established but require application dependent models to relate measured variables to film characteristics. Also, any control action based on a real-time layer characteristic measurement will demand a change in pressure or temperature (through the reference manager, for example), since

² Step coverage is achieved when all surface of a wafer has been covered.

³ Here, observable refers to the ability of reconstructing all state variables based on the given measured variables.

these are the variables that affect the chemical reactions during the depositions. We therefore consider such a controller to be of a higher hierarchical level than the partial pressure or temperature controllers in such a process. This causes its effectiveness to be dependent on the performance of the lower level pressure and temperature controllers. In contrast to the above, a method for measuring the precursor partial pressures (the third measured state variable) is not clearly visible in the literature and it will constitute one of main contributions of this paper. Particularly, we will present the design and experimental validation of a real-time partial pressure measurement sensor for UHVCVD.

The main techniques for real-time partial pressure or flux measurements that are suitable for vacuum conditions are mass spectrometry (MS) [21], electron impact emission spectrometry (EIES) [22] and atomic absorption spectrometry (AAS) [23–27]. Both MS and EIES are material specific and highly sensitive. However, they require physical presence of a sensor with a heated filament in the deposition chamber and the measurement is therefore intrusive and places restrictions on the thermal budget. Moreover, the sensor will need to be heated with the rest of the reactor, which will therefore restrict the thermal budget further. AAS is a very sensitive and selective atom detection technique that can operate at any pressure. It is furthermore non-intrusive and therefore places little constraints on the system design and thermal budget. This, combined with the (typical) atomic reactant presence in the deposition chamber makes the AAS measurement a suitable measuring technique for UHVCVD. The measurement can furthermore be related to the fluxes in the process since it provides a measure of the number of atoms in the optical path. Based on this consideration, we design an AAS-based real-time partial pressure sensor system which will be discussed in detail in Section 4.

3. Modeling for UHVCVD partial pressure control

Under vacuum condition, the pressure in a given volume satisfies the relation described by the ideal gas law

$$PV = NRT_a, \quad (1)$$

where P is the pressure, V is volume of interest, N is the number of moles inside the atom cloud, R is the ideal gas constant and T_a is the average temperature of the atom cloud. In order to obtain P , we are accordingly interested in determining N and T_a for the precursors of interest.

When we consider N , the simplest way of modeling it is by considering the deposition chamber as a single volume. In this case, the variable N can be modeled by

$$\dot{N}(t) = \dot{N}_{in}(t) - \dot{N}_s(t) - \dot{N}_{out}(t), \quad (2)$$

where \dot{N}_{in} and \dot{N}_{out} are respectively the number of moles per second entering and exiting the volume and \dot{N}_s is number of moles per second that gets sorbed (or negatively; desorbed) to surfaces in \mathbb{M} , the set of 2-dimensional surface facing the atom cloud. It is a lump model that does not contain information on the flows occurring inside the volume of interest. As a result, it prevents us to gain insight on the temperature-sensitive and spatially-dependent sorption characteristics.

In the remainder of this section, we will present a modeling framework that allows for more realistic description of the flows inside the deposition chamber. Such a modeling framework was previously introduced in [28] and in this work we consider an adaptation of the previously presented result.

3.1. Modeling framework

For a given geometry containing a FMF regime, we are interested in the evolution of fluxes over time through a spatial discretization of the inner surface of the geometry. Let us discretize the geometry in n -elements. We further consider an incoming flux that can be manipulated by a controller and we define the partial pressure as the

output variable. For the flux evolution (without leakage) we consider the relation

$$x^+(t) = p^A(x(t) - \dot{s}(t) + G(u(t), t)), \quad (3)$$

where $x^+(t) \in \mathbb{R}^n$ is the flux magnitude at each discretized elements after a (small) time step, $p^A \in \mathbb{R}^{n \times n}$ is a constant symmetric matrix describing scattering of the fluxes between surfaces in accordance with the Knudsen cosine law [28,29], $x(t) \in \mathbb{R}^n$ is the flux magnitude, $\dot{s}(t)$ is the change in moles sorbed to the considered surface and $G(u, t)$ is the flux magnitude change caused by new precursor evaporation to each element in the inner surface. Consequently, we consider the spatially discretized model as follows

$$\begin{aligned} \dot{x}(t) &= (A - \delta I - L)x(t) - (A - L)(f(x(t), s(t), T(t)) - g(u(t), t)), \\ \dot{z}(t) &= f(x(t), s(t), T(t)), \\ \dot{s}(t) &= z(t), \end{aligned} \quad (4)$$

$$y(t) = h(x(t), T_a(t)) = \frac{R}{V} \sqrt{\frac{T_a(t) \pi M}{8R}} \mathbb{1}^\top (p^A \cdot \ell) x(t),$$

where \cdot is element-wise multiplication. In (4), the state $x(t) \in \mathbb{R}^n$ represents atomic fluxes (in moles per second) on discrete surface areas $\{\omega_1, \omega_2, \dots, \omega_n\} \in \mathbb{M}$, $z(t)$ is the derivative of $s(t)$, where $s(t) \in \mathbb{R}^n$ represents particles that are sorbed to the same collection of surfaces as considered for $x(t)$. The matrix $A \in \mathbb{R}^{n \times n}$ describes the particle transfers that are calculated based on the Knudsen cosine law, between all pairs of the n discrete surfaces, satisfying $\sum_i A_{i,j} = \delta$, for $j = 1, \dots, n$. Here, $\delta \in \mathbb{R}_{\geq 0}$ is a constant that corrects for the time scale of the particle transfer phenomena and $A = \delta p^A$. The matrix $L \in \mathbb{R}_{\geq 0}^{n \times n}$ incorporates the leakage from the deposition chamber. The function $f(x(t), s(t), T(t))$ produces a n -dimensional vector that describes the non-linear sorption and desorption phenomena for each of the n discrete surfaces. These effects are subject to changes in the temperature and the chemical compositions of the surfaces. The input function $g(u(t), t)$ produces a n -dimensional vector that (non-linearly) relates the controlled input(s) $u(t) \in \mathbb{R}^m$ to fluxes directed at the n discrete surfaces. The time dependence represents changes in flux source characteristics. For the output $y(t)$, we have the function $h(x(t), T_a(t))$ that relates the fluxes to the partial pressure. The variable T_a is the average temperature of the atom cloud, M is the moles mass of the element of interest, R is the gas constant, $\mathbb{1}$ is a n -length column vector of ones and $\ell \in \mathbb{R}^{n \times n}$ a symmetric matrix containing average path lengths of the fluxes through the volume V , where the (i, j) th entry corresponds to the path length from surface i to surface j . We will use the upcoming subsections to discuss the various components more extensively.

Notice that when we take $n = 1$, (2) and (4) are very similar. More precisely, for (4) we obtain the simplified case with $A = \delta$ and we have

$$N = xv^{-1}\ell, \quad (5)$$

with v the average speed of the atoms. For a constant v we then obtain

$$\dot{N} = \dot{x}v^{-1}\ell. \quad (6)$$

Accordingly, with respect to (2), we have $\dot{N}_{out} = v^{-1}\ell Lx(t)$, $\dot{N}_{in} = v^{-1}\ell g(u(t), t)$ and $\dot{N}_s = v^{-1}\ell f(\cdot)$.

3.2. Transfer matrix A and leakage matrix L

We obtain the matrix A in two steps: (i) we derive a matrix p^A based on the Knudsen cosine law; and (ii) we scale p^A by a factor δ to obtain A .

For (i), we can determine the particles transfer matrix p^A analytically by calculating the area integration of the Knudsen cosine law explicitly, or through an approximation based on numerical integration. The latter can also be realized through sampling/randomization methods. In general, and with reference to Fig. 2, the (i, j) th element of p^A

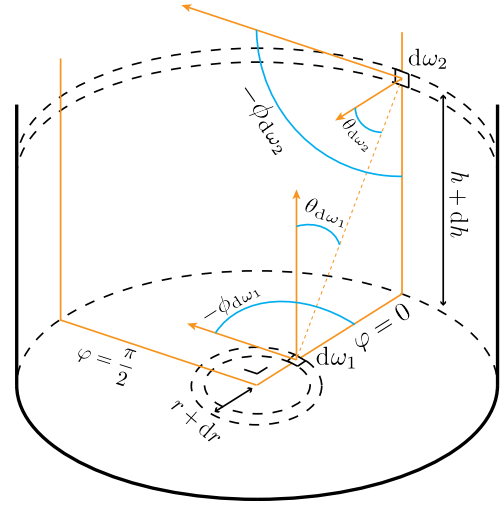


Fig. 2. A graphical interpretation of coordinates used in the Knudsen cosine law is shown. The considered infinitesimal areas are labeled as $d\omega_1$ and $d\omega_2$. Their relative locations are expressed in angles θ and ϕ belonging to each of the infinitesimal areas. φ represents the relative rotation around the central axis of the cylinder.

(which corresponds to the particles transfer between discrete surfaces ω_i and ω_j) is obtained by solving

$$p_{i,j}^A = \int_{\omega_j} \int_{\omega_i} \frac{\cos(\theta_{d\omega_i}) \cos(\theta_{d\omega_j})}{\text{dist}(d\omega_i, d\omega_j)^2 \pi} d\omega_i d\omega_j. \quad (7)$$

It follows that p^A is symmetric and we have $\sum_i p^A(i, j) = 1$, for all j . We remark that for the simple case where a cylinder is considered and is discretized only along the radius or the height, we have an analytic expression of p^A which is presented in [30].

Instead of analytically solving the Knudsen cosine law between different discrete spaces in a given geometry, we can approximate p^A through a sampling method, e.g., Monte Carlo (MC) simulation, as is commonly used in the literature on such processes. In [28] we have discussed how to set up such sampling method for approximating p^A on an arbitrary geometry. We have furthermore validated this approach by comparing it with the analytic computation for the simple cylinder geometry as given in [30]. Solving the Knudsen cosine law explicitly yields the most accurate solution. However, obtaining this solution quickly becomes non-trivial for finer discretizations or more complex geometries. On the other hand, approximating through sampling remains fairly straightforward for fine discretizations and this approach allows us to deal with the more complex geometries that we encounter in real applications of, for example, UHV/CVD reactor design.

For (ii), we need to scale p^A by a constant factor δ in order to obtain A . Here, δ represents a timescale correction for the scattering phenomena. Indeed, the speed of the dynamics is not directly apparent as it can be dependent on multiple physical factors that are difficult to characterize, such as atomic vibration time and binding energy. The parameter δ can be fitted empirically.

It is typically desirable to have designed leakage in vacuum processes, we therefore incorporate the leakage in the model. In our model (4), the leakage is encapsulated in the matrix L .

3.3. Sorption function vector $f(x, s, T)$

The sorption function vector has the primary purpose of incorporating the changes in fluxes that occur through sorption phenomena. For adsorptions and desorptions, there are generally two ways to obtain such a function: (i) by considering the physical laws that describe adsorption and desorption, or (ii) by considering the semi-empirical vapor pressure functions. The function $f(\cdot)$ should ideally satisfy the dynamics described by both. Notice that the function $f(\cdot)$ in fact

complements the sorption already described by A . Indeed, the Knudsen cosine law is described to hold for weakly absorbing (or adsorbing) and rough surfaces. Some of the sorption dynamics are accordingly inherited through application of the Knudsen cosine law.

3.4. Input function $g(u, t)$

The input function $g(\cdot)$ relates the input u to the fluxes x . Here, $u(t)$ is typically applied electric current which in turn heats up an evaporation source. When the evaporation source is active, it loses mass and its behavior will therefore change over time. The evaporation sources are typically subject to variations. The variations can possibly be dealt with by either explicit characterization, modeling and control for this variation (through methods as presented in [31]) or by implementation of traditional feedback control for the evaporated material partial pressures.

3.5. Output function $h(x, T)$

The output function $h(\cdot)$ serves to relate the states x (and optionally s) to an estimated pressure y , so that it can be compared to the measured pressure P . Using the same reasoning as in the introduction of this section, we can use (1) to relate an estimate on the number of moles in a volume V , denoted by N to the estimated pressure y . Eq. (1) accordingly becomes

$$y = \frac{NRT_a}{V}. \quad (8)$$

For obtaining N , we can use our knowledge on the flux magnitudes on the surfaces. This relation is then given by

$$N = \frac{1}{v} \mathbf{1}^\top (q \cdot \ell) \mathbf{1}, \quad (9)$$

where \cdot is an element-wise multiplication, N is in moles, v is the average atom speed in meters per second, $q \in \mathbb{R}^{n \times n}$ is the directed fluxes (from surface i to j) in moles per second and $\ell \in \mathbb{R}^{n \times n}$ is a symmetric matrix containing the corresponding path lengths of the fluxes through V in meters.

We can approximate q by using the information on how strongly each surface contributes to the total flux on any other surface, which is stored in A , or more precisely, in p^A . We approximate the fluxes between surfaces accordingly through

$$q = p^A \cdot (\mathbf{1}x^\top), \quad (10)$$

where $\mathbf{1}$ is an n -length column vector of ones.

For ℓ , we take the average path length through the volume of interest V , between all pairs of surfaces. We accordingly have that the (i, j) th entry of ℓ corresponds to the path lengths between the surfaces ω_i and ω_j . The matrix is furthermore symmetric since this length is not dependent on direction.

The mean speed of the atoms v can be obtained from the Maxwell-Boltzmann distribution and is given by

$$v = \sqrt{\frac{8RT_a}{\pi M}}, \quad (11)$$

with R the gas constant in Joules per mole Kelvin, T_a the average temperature of the atom cloud in Kelvin and M moles mass in kilograms per mole.

The output function in (4) is accordingly obtained by combining Eqs. (8)–(11).

3.6. Observability properties of the fluxes model

Let us now shortly discuss the observability property of the fluxes model introduced in this section. The model is nonlinear due to the time dependence of the temperature terms $T(t)$ and $T_a(t)$ and the functions $f(\cdot)$ and $g(\cdot)$. For the latter, we have not assumed a specific structure but analytic methods to assess the observability for system with nonlinear vector fields are well established for smooth affine nonlinear systems. On the one hand, if the functions $f(\cdot)$ and $g(\cdot)$ are linear then one can

immediately test the observability of the resulting linear systems with the inputs u , T and T_a , and the output y . On the other hand, when (4) is assumed to be affine time-invariant nonlinear systems, e.g., $g(u(t), t) = Bu(t)$, then one can evaluate the observability rank condition from the geometric control theory as expounded in [32]. Detailed analysis of the conditions for observability is beyond the scope of this work.

4. Experimental design and setup & AAS-based sensor system design and modeling

In this section we will describe our experimental scope and setup, the AAS sensor design and calibration, simplifications and assumptions we make and how we apply the modeling framework that we have presented in Section 3. We restrict the scope of the experiment to the vapor pressure regime. This has the advantage that: (i) we can use existing vapor pressure functions for derivation of the sorption functions $f(\cdot)$ and $\tilde{N}_s(\cdot)$, (ii) we can perform the assessment of the AAS sensor and the models simultaneously, and (iii) we can proceed without identifying the function $g(\cdot)$ described in Section 3.4.

4.1. Experimental setup design

The experimental setup is shown in Fig. 3. We consider sodium as the precursor material as it is well-studied and has a relatively high vapor pressure. The setup consists of three layers. The first and outermost layer is the thermal layer, which functions as an oven. This layer facilitates the hot wall processing and high temperature cleaning of the reactor, which is required for obtaining UHV conditions. The second layer is the vacuum layer. The vacuum layer is formed by a stainless steel vacuum chamber, which is attached to the vacuum pumps. The vacuum layer is outfitted with various viewports and feedthroughs for signal interaction. The third and innermost layer is the chemical layer. The chemical layer allows for building up of sodium pressure by providing an environment with a desired leakage (e.g. such that the sodium cannot be pumped away easily). Such a layer is often referred to as the deposition chamber and is located inside the vacuum. The set \mathbb{M} is the inside surface of this chamber for this experiment. We use a glass cylinder as deposition chamber for our experiments. This chamber furthermore facilitates mounting of the sodium evaporation sources.

The design facilitates the following real-time measurements: (i) reactor temperatures, (ii) cooling element temperature, (iii) sodium pressure and (iv) pump pressure. The temperatures are measured with K-type thermocouples, the sodium pressure is measured through AAS (whose design we present in Section 4.2) and the pump pressure is measured with a hot-filament ionization gauge. Read-out is done with modules supplied by National Instruments (NI USB-6211) for the pressures and Measurement Computing (MC USB-TC) for the temperatures. All measured signals are handled and manipulated in Labview.

The following actuators are used: (i) heating elements forming the thermal layer, (ii) sodium evaporation sources, (iii) a proportional pressure valve connected to the cooling element and (iv) pressure pumps. The heating elements are part of a separate PID control loop so that we can directly control the temperature of the thermal layer. These heating elements allow for heating above 600 degrees Kelvin everywhere inside the thermal layer. The sodium source is current controlled and the current is set directly. The cooling element air flow is controlled with a proportional valve (Festo VEAB). This flow is regulated with a proportional controller so that we can set the cold spot temperature as an input. We use a diaphragm pump and a turbo molecular pump (both Pfeiffer) to attain the UHV conditions. The pumps allow for pressures $< 10^{-7}$ Pa after bake-out. The actuation signals are generated in Labview and applied with the previously mentioned NI USB-6211 module and the MC USB-3103 module of Measurement Computing.

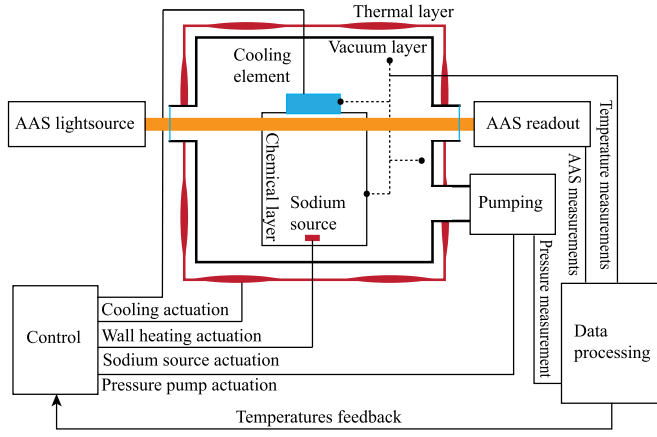


Fig. 3. A schematic of the experimental setup used in this paper is shown. The setup consists of three fundamental layers, which act as boundaries for the temperature (thermal layer), the pressure (vacuum layer) and for the sodium atoms (chemistry layer). The design allows for real-time measurements of temperature, reactor pressure and sodium pressure (through AAS). The AAS components are discussed in more detail in Section 4.2. The setup actuators are the pressure pumps, the sodium source, the wall heating elements and the cooling element. The cooling element is placed so that it directly influences vapor pressures inside the chemistry layer.

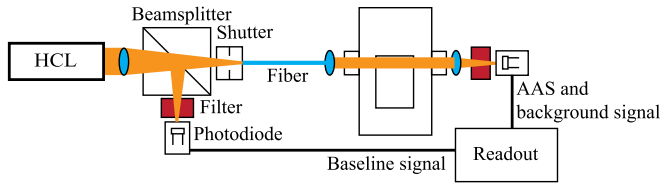


Fig. 4. A schematic representation of the AAS sensor design is shown. The AAS light source is a hollow cathode lamp (HCL). The light generated by this lamp is focused and sent through a beamsplitter. From there, one of the bundles is filtered and converted to an electronic signal. This signal is the baseline signal. The other bundle is sent through a shutter and into an optical fiber. This light is subsequently focused through the deposition chamber, which contains the atom cloud. After this, the light is filtered and converted to an electronic signal. This signal is the AAS signal when the shutter is open and the background signal when the shutter is closed. The AAS sensor is integrated in the setup shown in Fig. 3.

4.2. AAS design, signal processing and calibration

The full AAS sensor design is shown in Fig. 4. The design features a dual beam setup (as in [27]), to correct for changes in light intensity generated by the lamp, and a shutter, to correct for changes in background light intensity. As light source we use a sodium hollow-cathode lamp supplied by Hamamatsu.

For such an AAS setup we can use a modification of the formulas provided in [27]. Accordingly, we have for very low fluxes and under monochromatic radiation the Beer–Lambert law for absorbance given by

$$\lambda(t) = \log_{10} \left(\frac{Q_{in}(t)}{Q_{out}(t)} \right) \propto \frac{N(t)Lk}{V}, \quad (12)$$

where λ is the absorbance, Q_{in} is the light intensity entering the atomic cloud, Q_{out} is the light intensity exiting the atomic cloud, N is the relevant number of atoms inside the volume of interest V , L is the length of the absorbing path and k is the absorbing coefficient. We remark that k is constant for a constant light frequency, as in our AAS setup.

Let us first determine a way to estimate the intensity of light entering the reactor Q_{in} . We would like this quantity to incorporate

all the light loss resulting from the optic components. Accordingly, we take upon initialization

$$Q_{in}(0) = Q_{out}(0) = Q_s(0) - Q_b(0),$$

where Q_s is the measured light with the shutter opened, Q_b is the measured background light with the shutter closed. For the future quantification of this incident light intensity we can then use

$$Q_{in}(t) = \frac{Q_{in}(0)}{Q_{ref}(0)} Q_{ref}(t), \quad (13)$$

where Q_{ref} refers to the measured baseline intensity. For the propagation of $Q_{out}(t)$, we use

$$Q_{out}(t) = Q_s(t) - Q_b(t). \quad (14)$$

Combining (12), (13) and (14) accordingly yields

$$\lambda(t) = \log_{10} \left(\frac{Q_{in}(0)Q_{ref}(t)}{Q_{ref}(0)(Q_s(t) - Q_b(t))} \right). \quad (15)$$

The next step is to relate the absorbance of light to the sodium pressure, e.g. to perform the calibration. Let us consider a mapping $\Lambda = \Psi(\lambda)$, with Λ the measured sodium pressure in Pa. We obtain $\Psi(\cdot)$ by actively controlling the vapor pressure in our experimental setup through the temperature of the cooling element. It can be checked that the vapor pressure is primarily determined by the coldest surface, which essentially acts as an atom trap. The change in pressure is furthermore nearly instantaneous, because of the significantly smaller time scale of mass transport and sorption phenomena. For sodium, we can use the vapor pressure relation [33]

$$P_{Na} = \xi(T_c) = 133.322 \times 10^{7.4925 - \left(\frac{5370}{T_c}\right)}, \quad (16)$$

with P_{Na} the sodium pressure in Pascal and T_c the cold spot temperature in Kelvin. We can accordingly approximate the function $\Psi(\cdot)$ from the datasets.

4.3. Other design choices, simplifications and assumptions

In order to maintain the vapor pressure regime inside the deposition chamber, we design the deposition chamber with minimal leakage. And, as mentioned in the introduction of this section, we can restrict ourselves to the situation where no new evaporations occur for this experiment. This implies that, with reference to (4), we have that $L \approx 0$ and $g(u(t), t) = 0$. We accordingly obtain simplified dynamics which allow us to focus on the role of A and $f(\cdot)$. The model can, at a later stage, be extended to include L and $g(u(t), t)$, using the insights we obtain on A and $f(\cdot)$ in this paper.

We have accordingly allowed ourselves to eliminate the original input $u(t)$. However, our experimental setup features direct control over the cold spot temperature T_c . We can accordingly consider a new input $\tilde{T}_r = \hat{u}(t)$, where T_r is a temperature reference signal supplied to the cold spot. For T_a , we expect that the average temperature in the atom cloud will satisfy a weighted average temperature of the surface facing the atom cloud. The weight is dependent on residence time on each surface, and cold surfaces will therefore have a stronger influence on the temperature than hot surfaces. For ease of reasoning, we will assume that $T_a = T_c$. We will furthermore assume that the temperatures of the surfaces facing the atom cloud, other than the temperature of the cold spot, are constant.

In the vapor pressure regime, a bulk material of precursor atoms are present on the coldest surface of the reactor. Such a bulk material will by approximation have a constant number of atoms that are exposed to the vacuum, depending on surface area, roughness and porosity. Furthermore, only atoms exposed to the vacuum can desorb from this bulk material. This phenomena causes a decoupling of the dynamics of x and s through $f(\cdot)$, since s will be represented in $f(\cdot)$ through a saturation function which is consequently saturated in the vapor pressure regime. Moreover, the vapor pressure function (16), which we will use as a starting point for deriving $f(\cdot)$ and $\dot{N}_s(\cdot)$, does not directly provide required information on the sorption that occurs. We will accordingly not incorporate s as a state for this experiment.

4.4. Model implementation for experiment

The simplifications and assumptions that we have discussed in the previous section have direct implications on the modeling for our experiment. We will present our model implementation for the experimental setup here. To assess our models performance, we will compare the fluxes model (as in (4)) with the moles model having N as state (as in (2)). We are now ready to derive a structure for the sorption functions $f(\cdot)$ and $\dot{N}_s(\cdot)$.

As shortly discussed in Section 4.3, we can derive a structure for the function $f(\cdot)$ using (16). The intermediate steps can be found in Appendix A. This procedure accordingly yields the structure

$$f(x, T_r) = \left[b_1 \frac{x}{T_r} + b_2 \frac{10^{\frac{b_3}{T_r}}}{T_r^{2.5}} \right] \hat{T}_r, \quad (17)$$

with b_1 , b_2 and b_3 to be fitted.

We will evaluate this model for $n = 4$. We discretize the cylinder as follows; ω_1 is the cylinder bottom, ω_2 the lower half of the side, ω_3 the upper half of the side and ω_4 the top. The reference temperature \hat{T}_r is accordingly associated with ω_4 . Notice furthermore that (17) is zero for a constant surface temperature, such as we assume for the surfaces ω_1 , ω_2 and ω_3 . We then obtain

$$\dot{x}(t) = (A - \delta I)x(t) - A \begin{bmatrix} 0 \\ 0 \\ 0 \\ 1 \end{bmatrix} \left[b_1 \frac{x_4(t)}{T_r(t)} + b_2 \frac{10^{\frac{b_3}{T_r(t)}}}{T_r(t)^{2.5}} \right] \hat{u}(t), \quad (18)$$

$$\hat{T}_r(t) = \hat{u}(t),$$

$$y(t) = \frac{2R}{V} \sqrt{\frac{T_r(t)\pi M}{8R}} \mathbb{1}^\top (p^A \cdot \ell)x(t),$$

where we consider only the top half of the cylinder volume for the ideal gas law part of $h(\cdot)$, e.g. 0.5 V.

For the moles model, we derive $\dot{N}_s(\cdot)$ in a similar fashion as we did $f(\cdot)$. The steps can be found in Appendix B. We accordingly have

$$\dot{N}_s(N, T_r) = \left[\frac{N}{T_r} + \frac{\alpha 10^{\frac{\beta}{T_r}}}{T_r^3} \right] \hat{T}_r, \quad (19)$$

where $\alpha = -7.5909 \times 10^9$ and $\beta = -5370$. We then have the full system as

$$\dot{N}(t) = \left[\frac{N(t)}{T_r(t)} + \frac{\alpha 10^{\frac{\beta}{T_r(t)}}}{T_r(t)^3} \right] \hat{u}(t), \quad (20)$$

$$\hat{T}_r(t) = \hat{u}(t),$$

$$\bar{y}(t) = \frac{N(t)RT_r(t)}{V}.$$

We will now discuss the numerical values of constants used in the models. The deposition chamber is a glass cylinder with a height of 0.102 m and a radius of 0.062 m. It accordingly has a total volume $V = 1.23 \times 10^{-3} \text{ m}^3$. We furthermore have the gas constant $R = 8.3145 \frac{\text{J}}{\text{mol K}}$ and the moles mass of sodium $M = 0.0230 \frac{\text{kg}}{\text{mol}}$. For ℓ , the path length (in meters) of the directed fluxes through V , we will suffice with a crude approximation. We accordingly let

$$\ell = \begin{bmatrix} 0 & 0 & 0.025 & 0.05 \\ 0 & 0 & 0.05 & 0.075 \\ 0.025 & 0.05 & 0.1 & 0.1 \\ 0.05 & 0.075 & 0.1 & 0.1 \end{bmatrix}. \quad (21)$$

For the described geometry, we follow the procedures described in Section 3.2 to obtain the matrix p^A . In this case, since our discretization is similar to the discretization used in [30], we can derive it from transfer probability functions provided there. The matrix p^A is accordingly

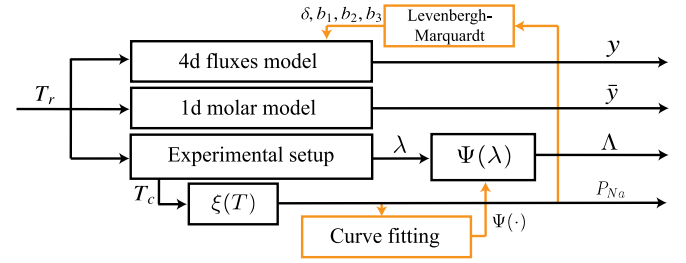


Fig. 5. We show the interaction of modeling components with our experimental setup. The experimental setup input $T_r = \hat{u}(t)$ is, together with its solution, also the input for the models. P_{Na} on the other hand, is determined from the measured cold spot temperature T_c . The orange parts in this diagram are the components used to fit the function Ψ and the parameters δ , b_1 , b_2 and c_3 , these parts are performed *ex situ*. The black parts in the diagram belong to main system and can run real-time. The purpose of the experiment is to obtain and compare the outputs \bar{y} , y , A and P_{Na} . The variable overview, where the measured variables are highlighted, is given in Table 1.

given by

$$p^A = \begin{bmatrix} 0 & 0.1373 & 0.3350 & 0.5277 \\ 0.1373 & 0.3300 & 0.1977 & 0.3350 \\ 0.3350 & 0.1977 & 0.3300 & 0.1373 \\ 0.5277 & 0.3350 & 0.1373 & 0 \end{bmatrix}, \quad (22)$$

We are then left with fitting the remaining parameters δ , b_1 , b_2 and b_3 . Such a fitting procedure is necessary, since the effect of A and δ on the sorptions is not directly clear (as discussed in Sections 3.2 and 3.3). We apply the Levenberg–Marquardt algorithm with $e(t) = P_{Na}(t) - y(t)$. For a smooth input signal $\hat{u}(t)$, we can obtain the reference temperature profile of the cold spot $T_r(t)$ in accordance with (18). This profile should be so that it covers the temperature domain of interest. The theoretical pressure inside the reactor can then be determined through (16), where we consider $P_{Na}(t) = \xi(T_r(t))$. The variable $y(t)$ is then the associated model output for this temperature profile. Using this procedure, we obtain $\delta = 0.8112$, $b_1 = 3.3230$, $b_2 = -2.9914 \times 10^{12}$ and $b_3 = -5378.5$. Lastly, we have $A = \delta p^A$.

The relation between all obtained variables and functions is shown in Fig. 5. In this figure, the orange parts relate to the system identification parts of the modeling. The black parts will be used to assess performance during the experimentation.

5. Experimental results and discussion

We are now ready to present our experimental results. To this end, we will first discuss our AAS sensor performance and calibration and how we obtain $\Psi(\cdot)$, followed by a comparison of the four sodium pressure signals depicted in Fig. 5. We evaluate the performance of the components by applying a sinusoidal reference temperature signal T_r to our cold spot. For this signal and its derivative we use

$$T_r(t) = 30 \cos\left(\frac{\pi t}{5400}\right) + 403.15, \quad (23)$$

$$\dot{T}_r(t) = -\frac{\pi}{180} \sin\left(\frac{\pi t}{5400}\right). \quad (24)$$

The applied and realized temperature profiles are shown in Fig. 6.

5.1. AAS sensor assessment and calibration

We assess the performance of our sensor by evaluating deviation in the measured absorbance between the three cycles shown in Fig. 6. The results are shown in Fig. 7. The deviation between the cycles is very small, indicating that the measurements are reproducible with small relative error. It is furthermore apparent that the graph displays the symmetry from the cold spot temperature reference (23). This confirms that we are operating strictly in the vapor pressure region and that the

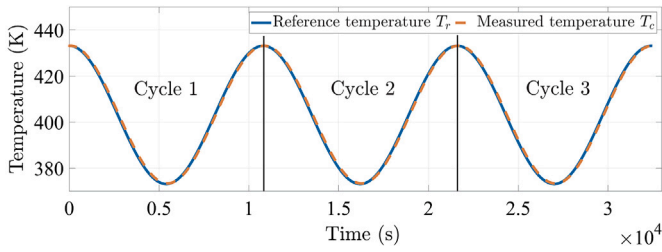


Fig. 6. The reference and realized cold spot temperature profiles are shown. The reference profile is generated in accordance with (23) and (24). We can identify three cosine cycles applied during the experiment, which we will compare to investigate measurement reproducibility. The graph furthermore shows that the applied proportional control loop is able to track the reference with a small delay. The length of the cosine cycle is determined by physical constraints, where in particular the heating of the cold spot is rate restricted since we only control the flow of a cooling air stream to this part of the reactor.

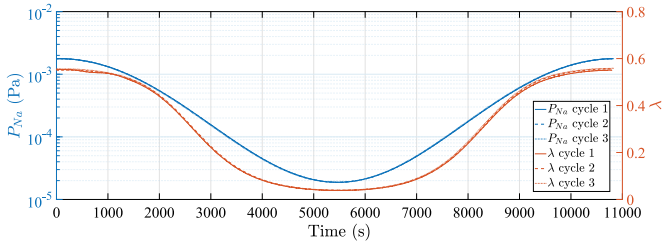


Fig. 7. We show the measured absorbance (λ) and derived vapor pressure ($P_{Na} = \xi(T_c)$) evolution over time for the three cosine temperature cycles depicted in Fig. 6. The measurement results feature excellent reproducibility, which is apparent because the subsequent cycles are very close to each other.

pressures shown in Fig. 7 are good estimations of sodium pressure in the reactor.

The relation between the absorbance λ , the sodium pressure P_{Na} and the cold spot temperature T_c is shown more explicitly in Fig. 8. Based on the Beer–Lambert law (12) and the ideal gas law (1), we would expect the relation between λ and P_{Na} to satisfy

$$P_{Na} \propto \frac{\lambda L k R T_a}{V^2}, \quad (25)$$

where L , R and V are constants and k , the absorbing coefficient, is constant for constant light frequencies, which holds for this experiment. The temperature of the atom cloud T_a is the only factor that could cause the non-proportionality of the function shown in Fig. 8, according to (25). However, dividing the pressure by the cold spot temperature T_c , which should then possibly cause an over-correction due to the relatively strong temperature changes, does not yield a proportional slope. These results accordingly show that there is a discrepancy between the combined Beer–Lambert law (12) and ideal gas law (1) on the one side, and the sodium vapor pressure equation (16) on the other side. It is likely that the semi-empirical function (16) is the main cause of this, as there are multiple candidate forms for such functions and problems with experimental apparatus compromising the accuracy of obtained results are frequently reported in [33]. Perhaps the methods developed and applied in this paper can be used to improve understanding on this issue in the future.

As discussed above and shown in Fig. 8, the mapping $\Psi : \lambda \rightarrow \Lambda$ cannot be described by a simple proportional relation. We will therefore use a polynomial mapping instead. Such a mapping can easily be fitted to the data. We will use

$$\Psi(\lambda) = 7.138\lambda^7 - 12.29\lambda^6 + 8.498\lambda^5 - 3.005\lambda^4 + 0.5775\lambda^3 - 0.05822\lambda^2 + 0.003415\lambda - 5.495 \times 10^{-5}, \quad (26)$$

which holds for $\lambda \in [0.0375, 0.56]$. Function (26) is shown graphically in Fig. 8.

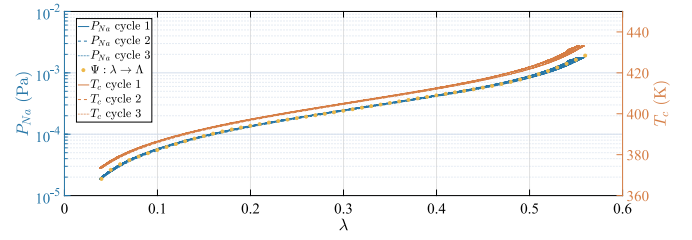


Fig. 8. We show the relations between the measured absorbance λ , the pressure P_{Na} and the temperature of the cold spot T_c . We furthermore show the function $\Psi : \lambda \rightarrow \Lambda$, for $\lambda \in [0.0375, 0.56]$, as in (26). The relation between the absorbance and the temperature depicted here only holds in the vapor pressure regime. The relation between the absorbance and the pressure holds outside this regime as well.

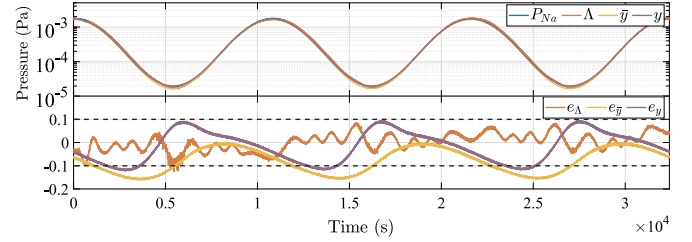


Fig. 9. We show a comparison between the theoretical vapor pressure P_{Na} , the measured vapor pressure Λ , the estimated vapor pressure from the moles model \bar{y} and the estimated vapor pressure from the fluxes model y . The normalized absolute errors $e_A = \frac{\Lambda - P_{Na}}{P_{Na}}$, $e_{\bar{y}} = \frac{\bar{y} - P_{Na}}{P_{Na}}$ and $e_y = \frac{y - P_{Na}}{P_{Na}}$ are shown in the lower graph. The dashed lines mark one order of magnitude error with P_{Na} . Residual errors are expected to be present because we use relatively low complexity lumped models that do not contain the full accuracy and complexity of the ‘real’ temporal and spatial dynamical phenomena.

5.2. Comparison of theoretical vapor pressure, model and sensor performance

We are now ready to compare the sodium pressure signals P_{Na} , Λ , \bar{y} and y . We initialize the simulations so that $y(0) \approx \bar{y}(0) \approx P_{Na}(0) = \xi(433.15)$. The four signals are shown in Fig. 9. We furthermore show three errors that take P_{Na} as a benchmark; $e_A = \frac{|\Lambda - P_{Na}|}{P_{Na}}$, $e_{\bar{y}} = \frac{|\bar{y} - P_{Na}|}{P_{Na}}$ and $e_y = \frac{|y - P_{Na}|}{P_{Na}}$.

Fig. 9 shows that all errors are significantly smaller in magnitude than the pressure P_{Na} that is being evaluated. Residual errors are expected to be present because we use relatively low complexity lumped models that do not contain the full accuracy and complexity of the ‘real’ temporal and spatial dynamical phenomena. We furthermore see that the accuracy of the measurement Λ is in the same range as the accuracy for the 1d moles model output \bar{y} and the 4d fluxes model output y . The results accordingly show that all three obtained signals are suitable for estimations of the sodium pressure P_{Na} . We can thus use the measurement Λ in combination with either the moles model or the fluxes model as a starting point for UHVCVD partial pressure controller design.

5.3. Discussion of fluxes model state estimations

Let us lastly discuss the flux magnitudes on the discrete surfaces of our cylinder, e.g. x_1, x_2, x_4 and x_4 . These flux magnitudes are shown in Fig. 10 for the course of the experiment. It is immediate to see that there are no significant differences in flux magnitudes compares to the changes that are induced by the heating and cooling of the cold spot temperature T_c . Any minor differences between the fluxes would in this case directly be inherited from p^A , which dictates the equilibrium for this experiment implementation when there are no changes in T_c . Another aspect that is apparent is that the scattering of fluxes through the cylinder occurs at a much faster timescale than the temperature

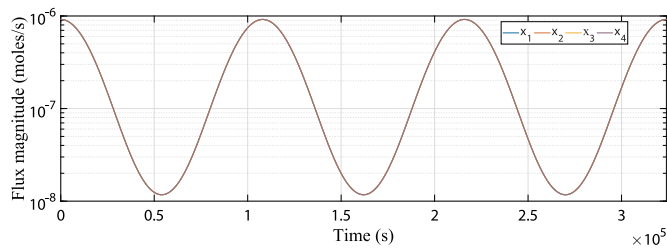


Fig. 10. We show the state estimates of the fluxes model for our experiment. Changes in moles of precursor that are sorbed to the cold spot instantly result in a new equilibrium of fluxes on the four surfaces due to the time-scale difference of the relevant phenomena. In this example any offset between the surfaces (which is induced through p^A) is negligible compared to the effect that the temperature changes have on the flux magnitudes.

changes of the cold spot, as changes in flux magnitudes occurs for all four fluxes at once, while the input term of the model only affects the flux on a single surface (x_4).

6. Conclusions

The work presented in this paper has provided the first steps in realizing an observable UHVCVD process. To this end, we have presented: (i) a conceptual control diagram, (ii) AAS sensor selection for real-time *in situ* partial pressure measurements, (iii) a fluxes model suitable to connect the reactor inputs and partial pressure measurements, (iv) experimental reactor design for validation purposes and (v) experimental results validating the AAS measurement, the output of the fluxes model and the output of the moles model in the vapor pressure regime.

Our experimental results indicate that the AAS sensor provides suitable measurements for controller design, having an error with the theoretical vapor pressure inside the reactor of magnitude significantly smaller than the magnitude of the pressure. We furthermore found that, when modeling the evolution of the vapor pressure, both the moles model and the fluxes model can provide estimations of the pressure with similar accuracy. Here, the moles models has an advantage of simplicity, while the fluxes model offers insight in fluxes inside the reactor. This insight can be particularly beneficial when modeling chemical reactions occurring at the substrate. We have accordingly provided the groundwork for future contributions on mechatronic system and control design and implementation for UHVCVD. It furthermore highlights the efficacy of the mechatronics design approach through improved reproducibility.

Future work may consider the observability and controllability properties and conditions for the fluxes model. We expect that this will particularly be insightful when a structure for the $f(\cdot)$ and $g(\cdot)$ functions is established. Determining a suitable structure for $f(\cdot)$ and $g(\cdot)$ for a set of specific applications is another topic of interest in its own right. Another direction for future work is validation of the fluxes model state estimation, which could not be performed with the experimental setup presented in this work. A future experiment that may facilitate further validation of the fluxes model could consider a dual chamber geometry, where two volumes are only connected via a small opening so that significant pressure gradients, and thus flux magnitude gradients, can occur.

CRedit authorship contribution statement

M. Dresscher: Lead investigator for this work. **B. Jayawardhana:** Involved as day-to-day supervisor. **B.J. Kooi:** Involved in advisory capacity, Representing their own backgrounds and fields. **J.M.A. Scherpen:** Involved in advisory capacity, Representing their own backgrounds and fields.

Declaration of competing interest

The authors declare that they have no known competing financial interests or personal relationships that could have appeared to influence the work reported in this paper.

Appendix A. Obtaining the sorption function $f(\cdot)$

We require f to be so that the fluxes x satisfy

$$P_{Na} = h(x, T_a),$$

for all t , with T_a the average temperature of the atom cloud and P_{Na} in Pascal. Indeed, for our experiment with only sodium present inside the reactor, no leakage and no evaporation, $f(\cdot)$ acts as a function that includes the vapor pressure phenomena in the dynamics. The vapor pressure can be related to temperature by empirical functions. Let us accordingly consider the function $\xi(T_c)$ from (16). We then have the requirement

$$\xi(T_c) = h(x, T_a),$$

or equivalently;

$$\frac{\partial \xi(T_c)}{\partial T_c} \dot{T}_c = \frac{\partial h(x, T_a)}{\partial x} \dot{x} + \frac{\partial h(x, T_a)}{\partial T_a} \dot{T}_a.$$

Rewriting yields

$$\frac{\partial h(x, T_a)}{\partial x} \dot{x} = \frac{\partial \xi(T_c)}{\partial T_c} \dot{T}_c - \frac{\partial h(x, T_a)}{\partial T_a} \dot{T}_a.$$

We consider a simplified case with $n = 1$, $g(u(t), t) = 0$ and $L = 0$. By substitution of \dot{x} with (4), we obtain

$$-\frac{\partial h(x, T_a)}{\partial x} \delta f(x, T) = \frac{\partial \xi(T_c)}{\partial T_c} \dot{T}_c - \frac{\partial h(x, T_a)}{\partial T_a} \dot{T}_a$$

Let us then denote

$$\zeta = \frac{R}{V} \sqrt{\frac{\pi M}{8R}} \ell.$$

We obtain for the partial derivatives

$$\begin{aligned} \frac{\partial h(x, T_a)}{\partial x} &= \zeta \sqrt{T_a}, \\ \frac{\partial h(x, T_a)}{\partial T_a} &= \frac{\zeta}{2\sqrt{T_a}} x(t), \\ \frac{\partial \xi(T_c)}{\partial T_c} &= \frac{a_1 10^{\frac{a_2}{T_c}}}{T_c^2}, \end{aligned}$$

with $a_1 = 5.1238 \times 10^{13}$ and $a_2 = -5370$. Care needs to be taken with the function ξ . Indeed, this function is essentially a mapping from the coldest surface to the sodium pressure, meaning it will not hold for all surfaces regardlessly. Let us place an assumption of uniformity for the interpretation of ξ . This means, that we let all temperature T_c , T_a and T be equal to T . The interpretation is that the atoms in the cloud take the temperature of the surfaces, which are uniform. We accordingly obtain

$$\begin{aligned} -\frac{\partial h(x, T)}{\partial x} \delta f(x, s, T) &= \left[\frac{\partial \xi(T)}{\partial T} - \frac{\partial h(x, T)}{\partial T} \right] \dot{T}, \\ f(x, T) &= \left[-\frac{\partial h(x, T)}{\partial x} \delta \right]^{-1} \left[\frac{\partial \xi(T)}{\partial T} - \frac{\partial h(x, T)}{\partial T} \right] \dot{T}. \end{aligned}$$

Which, through substitutions of the partial derivatives, yields

$$f(x, T) = \left[-\frac{a_1 10^{\frac{a_2}{T}}}{\delta \zeta T^{2.5}} + \frac{x}{2\delta T} \right] \dot{T}$$

or equivalently

$$f(x, T) = \left[b_1 \frac{x}{T} + b_2 \frac{10^{\frac{b_3}{T}}}{T^{2.5}} \right] \dot{T},$$

where b_1 , b_2 and b_3 are to be fitted.

Appendix B. Obtaining the sorption function $\dot{N}_s(\cdot)$

This procedure is similar to the one used in Appendix A. We start out with

$$\xi(T) = \frac{NRT}{V},$$

which is based on the ideal gas law. Differentiating yields

$$\frac{\partial \xi(T)}{\partial T} \dot{T} = \frac{\dot{N}RT}{V} + \frac{NRT}{V}$$

$$\frac{a_1 10^{\frac{a_2}{T}}}{T^2} \dot{T} = -\frac{\dot{N}_s RT}{V} + \frac{NRT}{V},$$

with $a_1 = 5.1238 \times 10^{13}$ and $a_2 = -5370$. Solving for \dot{N}_s then yields

$$\dot{N}_s = \left[\frac{N}{T} + \frac{\alpha 10^{\frac{\beta}{T}}}{T^3} \right] \dot{T},$$

with $\alpha = -7.5909 \times 10^9$ and $\beta = -5370$

References

- Pierson HO. Handbook Of Chemical Vapor Deposition: Principles, Technology and Applications. William Andrew; 1999.
- Vlassiok I, Fulvio P, Meyer H, Lavrik N, Dai S, Datskos P, Smirnov S. Large scale atmospheric pressure chemical vapor deposition of graphene. Carbon 2013;54:58–67.
- Fay S, Steinhauer J, Nicolay S, Ballif C. Polycrystalline zno: B grown by LPCVD as TCO for thin film silicon solar cells. Thin Solid Films 2010;518(11):2961–6.
- Chowdhury I, Chandrasekhar M, Klein PB, Caldwell JD, Sudarshan T. High growth rate 4H-SiC epitaxial growth using dichlorosilane in a hot-wall CVD reactor. J Cryst Growth 2011;316(1):60–6.
- Miseikis V, Convertino D, Mishra N, Gemmi M, Mashoff T, Heun S, Haghghian N, Bisio F, Canepa M, Piazza V, et al. Rapid CVD growth of millimetre-sized single crystal graphene using a cold-wall reactor. 2D Mater 2015;2(1):014006.
- Ishizaki T, Hieda J, Saito N, Saito N, Takai O. Corrosion resistance and chemical stability of super-hydrophobic film deposited on magnesium alloy AZ31 by microwave plasma-enhanced chemical vapor deposition. Electrochim Acta 2010;55(23):7094–101.
- Liu Y, Gorla C, Liang S, Emanetoglu N, Lu Y, Shen H, Wraback M. Ultraviolet detectors based on epitaxial ZnO films grown by MOCVD. J Electron Mater 2000;29(1):69–74.
- Meyerson BS. Low-temperature silicon epitaxy by ultrahigh vacuum/chemical vapor deposition. Appl Phys Lett 1986;48(12):797–9.
- Greve D, Racanelli M. Growth rate of doped and undoped silicon by ultra-high vacuum chemical vapor deposition. J Electrochem Soc 1991;138(6):1744–8.
- Meyerson BS. UHV/CVD growth of Si and Si:Ge alloys: chemistry, physics, and device applications. Proc IEEE 1992;80(10):1592–608. <http://dx.doi.org/10.1109/5.168668>.
- Adam T, Bedell S, Reznicek A, Sadana D, Venkateshan A, Tsunoda T, Seino T, Nakatsuru J, Shinde S. Low-temperature growth of epitaxial (100) silicon based on silane and disilane in a 300mm UHV/CVD cold-wall reactor. J Cryst Growth 2010;312(23):3473–8.
- Cho AY, Arthur J. Molecular beam epitaxy. Progress in solid state chemistry 1975;10:157–91.
- Schlom DG, Chen L-Q, Pan X, Schmehl A, Zurbuchen MA. A thin film approach to engineering functionality into oxides. J Am Ceram Soc 2008;91(8):2429–54.
- Edgar TF, Butler SW, Campbell W, Pfeiffer C, Bode C, Hwang SB, Balakrishnan K, Hahn J. Automatic control in microelectronics manufacturing: Practices, challenges, and possibilities. Automatica 2000;36(11):1567–603.
- Wang Y, Gao F, Doyle FJ. Survey on iterative learning control, repetitive control, and run-to-run control. J Process Control 2009;19(10):1589–600.
- Middlebrooks SA, Rawlings JB. Model predictive control of $\text{Si}_{1-x}\text{Ge}_x$ thin film chemical-vapor deposition. IEEE Trans Semicond Manuf 2007;20(2):114–25. <http://dx.doi.org/10.1109/TSM.2007.895203>.
- Roozeboom F, Parekh N. Rapid thermal processing systems: A review with emphasis on temperature control. J Vacuum Sci Technol B 1990;8(6):1249–59.
- Holmqvist A, Törndahl T, Stenström S. A model-based methodology for the analysis and design of atomic layer deposition processes - Part I: Mechanistic modelling of continuous flow reactors. Chem Eng Sci 2012;81:260–72.
- Holmqvist A, Törndahl T, Stenström S. A model-based methodology for the analysis and design of atomic layer deposition processes - Part II: Experimental validation and mechanistic analysis. Chem Eng Sci 2013;94:316–29.
- Holmqvist A, Törndahl T, Stenström S. A model-based methodology for the analysis and design of atomic layer deposition processes - Part III: Constrained multi-objective optimization. Chem Eng Sci 2013;96:71–86.
- Chang L, Esaki L, Howard W, Ludeke R. The growth of a GaAs–GaAlAs superlattice. J Vac Sci Technol 1973;10(1):11–6.
- Lu C, Lightner M, Gogol C. Rate controlling and composition analysis of alloy deposition processes by electron impact emission spectroscopy (EIES). J Vac Sci Technol 1977;14(1):103–7.
- Klausmeier-Brown M, Eckstein J, Bozovic I, Virshup G. Accurate measurement of atomic beam flux by pseudo-double-beam atomic absorption spectroscopy for growth of thin-film oxide superconductors. Appl Phys Lett 1992;60(5):657–9.
- Lu C, Guan Y. Improved method of noninvasive deposition rate monitoring by atomic absorption spectroscopy for physical vapor deposition processes. J Vacuum Sci Technol A 1995;13(3):1797–801.
- Kasai Y, Sakai S. Atomic absorption spectroscopy system for flux monitoring and atomic-layer control of molecular beam epitaxial growth of bisrcauo. Rev Sci Instrum 1997;68(7):2850–5.
- Vignaud D, Mollot F. Real-time in-situ flux monitoring by wavelength-modulated atomic absorption spectroscopy in molecular beam epitaxy: Application to ga flux measurement. J Cryst Growth 2007;301:79–83.
- Du Y, Droubay TC, Liyu AV, Li G, Chambers SA. Self-corrected sensors based on atomic absorption spectroscopy for atom flux measurements in molecular beam epitaxy. Appl Phys Lett 2014;104(16):163110.
- Dresscher M, Jayawardhana B, Barradas-Berglind JJ, Scherpen JMA. A modeling framework and flux controller for free molecular flow deposition processes. In: 2017 American Control Conference, ACC. 2017, p. 2164–70. <http://dx.doi.org/10.23919/ACC.2017.7963273>.
- Knudsen M. The cosine law in the kinetic theory of gases. Ann Phys 1915;48:1113–21.
- Cale T, Raupp G. Free molecular transport and deposition in cylindrical features. J Vacuum Sci Technol B 1990;8(4):649–55.
- Dresscher M, Jayawardhana B. Prescribing transient and asymptotic behaviour to deterministic systems with stochastic initial conditions. Internat J Control 2020;1–14. <http://dx.doi.org/10.1080/00207179.2020.1774077>.
- Nijmeijer H, Van der Schaft A. Nonlinear dynamical control systems, vol. 175. Springer; 1990.
- Nesmeyanov AN. Vapor Pressure of the Chemical Elements. North-Holland; 1963.



Martijn Dresscher has received the B.Sc. in Technology Management in 2012, the M.Sc. Industrial Engineering and Management in 2014 and a Ph.D. in System and Control Engineering in 2019; all from the University of Groningen. His Ph.D. thesis was titled “Toward controlled ultra-high vacuum chemical vapor deposition processes”. He currently works at TNO in Delft, the Netherlands, as System Engineer. His main focus there is on optomechatronic system design for space.



Bayu Jayawardhana (IEEE Senior Member) received the B.Sc. degree in electrical and electronics engineering from the Institut Teknologi Bandung, Bandung, Indonesia, in 2000, the M.Eng. degree in electrical and electronics engineering from the Nanyang Technological University, Singapore, in 2003, and the Ph.D. degree in electrical and electronics engineering from Imperial College London, London, U.K., in 2006. He is currently a professor of Mechatronics and Control of Nonlinear Systems in the Faculty of Science and Engineering, University of Groningen, Groningen, The Netherlands.

He was with Bath University, Bath, U.K., and with Manchester Interdisciplinary Biocentre, University of Manchester, Manchester, U.K. His research interests include the analysis of nonlinear systems, systems with hysteresis, mechatronics, systems and synthetic biology. Prof. Jayawardhana is a Subject Editor of the International Journal of Robust and Nonlinear Control, an Associate Editor of the European Journal of Control and of IEEE Trans. Control Systems Technology and a member of the Conference Editorial Board of the IEEE Control Systems Society and of the European Control Association.



Bart J. Kooi studied Materials Science at Delft University of Technology and received his Ph.D. degree with Prof. Eric Mittemeijer in 1995 with a thesis titled “Iron-Nitrogen Phases: Thermodynamics, Long-Range Order and Oxidation Behavior”. Then he moved to the University of Groningen to work (since 1997) as an assistant and associate professor in the research group of Materials Science headed by Prof. De Hosson with a main focus on electron microscopy e.g. of metal-oxide interfaces. In 2001 he started research on phase-change materials for memory applications which developed

into a broader interest in chalcogenide materials. In 2009 he established his own research group “Nanostructured Materials and Interfaces” within the Zernike Institute for Advanced Materials, where he also started synthesis of nanomaterials using pulsed laser deposition and a dedicated nanocluster source based on magnetron sputtering and gas-phase aggregation. He participated, also as workpackage leader, in two European projects on phase-change memory and is currently chairman of the Annual European Phase-Change and Ovonic Science Symposium. He has published more than 190 articles in peer-reviewed journals (H-index 42 Google Scholar) with nanostructure–property relations as an overarching theme.



Jacquélien M.A. Scherpen received the M.Sc. and Ph.D. degrees in applied mathematics from the University of Twente, Enschede, The Netherlands, in 1990 and 1994, respectively. She was with Delft University of Technology, The Netherlands, from 1994 to 2006. Since September 2006, she is a Professor in the Engineering and Technology institute Groningen (ENTEG) of the Faculty of Science and Engineering, University of Groningen, Groningen, The Netherlands. She was Scientific Director of ENTEG from 2013 till 2019. She is now scientific director of the Engineering Center of the University of Groningen (GEC). She has held visiting research positions at the University of Tokyo, Japan, University de Compiegne, SUPELEC, Gif-sur-Yvette, France, and the Old Dominion University, Norfolk, VA, USA. Her current research interests include network model reduction methods, nonlinear model reduction methods, nonlinear control methods, modeling and control of physical systems with applications to electrical circuits, electromechanical systems and mechanical systems, and distributed optimal control applications to smart grids. Prof. Scherpen has been an Associate Editor of the IEEE TRANSACTIONS ON AUTOMATIC CONTROL, the International Journal of Robust and Nonlinear Control (IJRNC), and the IMA Journal of Mathematical Control and Information. She is currently on the Editorial Board of the IJRNC. She is elected member of the Board of Governors of the IEEE Control Systems Society (CSS), she is vice chair of the publication committee of the International Federation of Automatic Control (IFAC), and from 2020 to 2022 president of the European Control Association (EUCA).